The Dust and [C II] Morphologies of Redshift ∼4.5 Sub-millimeter Galaxies at ∼200 pc Resolution: The Absence of Large Clumps in the Interstellar Medium at High-redshift

B. Gullberg[1], A. M. Swinbank[1], I. Smail[1], A. D. Biggs[2], F. Bertoldi[3], C. De Breuck[2], S. C. Chapman[4], C.-C. Chen[2], E. A. Cooke[1], K. E. K. Coppin[5], P. Cox[6], H. Dannerbauer[7], J. S. Dunlop[8], A. C. Edge[1], D. Farrah[9], J. E. Geach[6], T. R. Greve[10], J. Hodge[11], E. Ibar[12], R. J. Ivison[2,8], A. Karim[13], E. Schinnerer[14], D. Scott[15], J. M. Simpson[16], S. M. Stach[1], A. P. Thomson[1,17], P. van der Werf[11], F. Walter[14], J. L. Wardlow[1], and A. Weiss[18]

[1] Centre for Extragalactic Astronomy, Department of Physics, Durham University, South Road, Durham DH1 3LE, UK
[2] European Southern Observatory, Karl-Schwarzschild-Straße 2, D-85748 Garching bei München, Germany
[3] Instituto de Astrofísica de Canarias (IAC), E-38205 La Laguna, Tenerife, Spain
[4] Department of Physics and Atmospheric Science, Dalhousie University, Halifax, Canada
[5] Centre for Astrophysics Research, Science & Technology Research Institute, University of Hertfordshire, Hatfield AL10 9AB, UK
[6] Joint ALMA Observatory—ESO, Av. Alonso de Cordova, 3104, Santiago, Chile
[7] Dpto. Astrofísica, Universidad de La Laguna, E-38206 La Laguna, Tenerife, Spain
[8] Institute for Astronomy, University of Edinburgh, Royal Observatory, Blackford Hill, Edinburgh EH9 3HJ, UK
[9] Department of Physics, Virginia Tech, Blacksburg, VA 24061, USA
[10] University College London, Gower Street, London WC1E 6BT, UK
[11] Leiden Observatory, Leiden University, P.O. Box 9513, 2300 RA Leiden, The Netherlands
[12] Instituto de Física y Astronomía, Universidad de Valparaíso, Avda. Gran Bretaña 1111, 2340000 Valparaíso, Chile
[13] Bonn University, Auf dem Hügel 71, D-53121 Bonn, Germany
[14] Max-Planck-Institut für Astronomie, Königstuhl 17, D-69117, Heidelberg, Germany
[15] Department of Physics & Astronomy, University of British Columbia, 6224 Agricultural Road, Vancouver, BC V6T 1Z1, Canada
[16] Academia Sinica Institute of Astronomy and Astrophysics, No. 1, Sec. 4, Roosevelt Road, Taipei 10617, Taiwan
[17] Jodrell Bank Centre for Astrophysics, The University of Manchester, Oxford Road, Manchester, M13 9PL, UK
[18] Max-Planck-Institut für Radioastronomie, Auf dem Hügel 69 D-53121 Bonn, Germany

Abstract

We present deep, high-resolution (0″03, 200 pc) ALMA Band 7 observations covering the dust continuum and [C II] $\lambda 157.7\,\mu m$ emission in four $z \sim 4.4$–4.8 sub-millimeter galaxies (SMGs) selected from the ALESS and AS2UDS surveys. The data show that the rest-frame $160\,\mu m$ (observed 345 GHz) dust emission is consistent with smooth morphologies on kpc scales for three of the sources. One source, UDS 47.0, displays apparent substructure, but this is also consistent with a smooth morphology—as indicated by simulations showing that smooth exponential disks can appear clumpy when observed at the high angular resolution (0″03) and depth of these observations ($\sigma_{345\,\mathrm{GHz}} \sim$ 27–47 μJy beam^{-1}). The four SMGs are bright [C II] emitters. We extract [C II] spectra from the high-resolution data, and recover ∼20%–100% of the [C II] flux and ∼40%–80% of the dust continuum emission, compared to the previous lower-resolution observations. When tapered to 0″2 resolution, our maps recover ∼80%–100% of the continuum emission, indicating that ∼60% of the emission is resolved out on ∼200 pc scales. We find that the [C II] emission in high-redshift galaxies is more spatially extended than the rest-frame $160\,\mu m$ dust continuum by a factor of 1.6 ± 0.4. By considering the $L_{\mathrm{[C II]}}/L_{\mathrm{FIR}}$ ratio as a function of the star formation rate surface density (Σ_{SFR}), we revisit the [C II] deficit and suggest that the decline in the $L_{\mathrm{[C II]}}/L_{\mathrm{FIR}}$ ratio as a function of Σ_{SFR} is consistent with local processes. We also explore the physical drivers that may be responsible for these trends and can give rise to the properties found in the densest regions of SMGs.

Key words: galaxies: evolution – galaxies: ISM – submillimeter: galaxies

1. Introduction

The most luminous galaxies at high redshift ($z > 1$) are dusty star-forming galaxies, originally identified at sub-millimeter wavelengths and therefore known as sub-millimeter galaxies (SMGs, Casey et al. 2014). This galaxy population has many properties similar to those of local ultra-luminous galaxies (ULIRGs, Sanders & Mirabel 1996), such as high infrared luminosities (typically $L_{\mathrm{FIR}} > 10^{12}\,L_{\odot}$), as well as high gas and dynamical masses and gas fractions (e.g., Tacconi et al. 2008; Engel et al. 2010; Riechers et al. 2011; Bothwell et al. 2013). However, studies have shown important differences between SMGs and ULIRGs. For example, the spatial extent of the gas and star formation in SMGs appears to be much larger than that typically seen in local ULIRGs (∼few kpc in SMGs compared to just hundreds of pc in local ULIRGs, e.g.,

Chapman et al. 2004; Sakamoto et al. 2008; Kennicutt et al. 2011; Croxall et al. 2012; Ivison et al. 2012; Ikarashi et al. 2015; Simpson et al. 2015a; Hodge et al. 2016), and while the intense star formation seen in local ULIRGs appears to be triggered by major mergers (e.g., Clements & Baker 1996; Farrah et al. 2001; Surace et al. 2001; Veilleux 2002), theoretical predictions have suggested that SMGs at $z \sim 1$–5 comprise a heterogeneous mix of star formation occurring in extended disks, pre-coalescence mergers, and late-stage mergers (e.g., Hayward et al. 2011; Cowley et al. 2017), which may be consistent with *Hubble Space Telescope* (*HST*) imaging (Chen et al. 2015).

Rest-frame ultraviolet (UV)/optical observations of high-redshift "main-sequence" star-forming galaxies show "clumpy" star-forming structures, more massive and brighter than seen

locally (e.g., Genzel et al. 2012; Livermore et al. 2012). In a simple framework for gas collapse in a gas-rich disk, the masses of these "clumps" are governed by the average gas surface density of the surrounding interstellar medium. In high-redshift galaxies with high gas fractions, the masses of collapsing clouds are therefore expected to be shifted to higher masses. This could result in 10^8–$10^9 M_\odot$ "clumps" (e.g., Förster Schreiber et al. 2011; Genzel et al. 2012; Livermore et al. 2012), and because more massive regions host proportionally more star formation (Kennicutt & Chu 1988), these giant clumps can dominate the galaxy morphology and thereby explain the clumpy nature of the UV/optical images of high-redshift galaxies (e.g., Elmegreen et al. 2009; Shibuya et al. 2015).

The resolution provided by ALMA is now allowing sub-millimeter observations on spatial scales comparable to those provided by optical and UV observations from *HST*. Recent studies have searched for giant clumps at sub-millimeter wavelengths (e.g., Swinbank et al. 2010, 2015; ALMA Partnership et al. 2015; Iono et al. 2016; Oteo et al. 2017). In a study of 16 ALESS SMGs at 0."16 resolution (∼1 kpc), Hodge et al. (2016) identified disk-like morphologies with no significant evidence for clumps in dust emission in the majority of their galaxies. However, giant H II regions in local galaxies are a few hundred parsecs across (e.g., Hill et al. 2005; Sakamoto et al. 2008). This means that, although this study measures structures on ∼1 kpc scales, even higher resolution is required to search for extended clumpy disks with 200–500 pc size clumps, as seen in some simulations (Dekel et al. 2009; Bournaud et al. 2014) and locally (e.g., Hill et al. 2005; Sakamoto et al. 2008).

One particularly powerful tool to study the structure of high-redshift galaxies in the sub-millimeter waveband is the bright [C II] $\lambda157.7\,\mu$m line. This far-infrared (FIR) fine-structure emission line is emitted by the $^2P_{3/2}$–$^2P_{1/2}$ transition in singly ionized carbon ([C II]) and accounts for up to ∼1% of the cooling in the interstellar medium (Stacey et al. 1991; Brauher et al. 2008; Graciá-Carpio et al. 2011). It is therefore one of the brightest and best-studied atomic lines. The [C II] emission line arises from both photo-dominated regions, which form on the UV-illuminated surfaces of molecular clouds, diffuse H II regions, and also from diffuse ISM (Madden et al. 1993; Lord et al. 1996). Early studies of [C II] in local ULIRGs using the *Kuiper Airborne Observatory* and *Infrared Space Observatory* (*ISO*) (Stacey et al. 1991; Malhotra et al. 1997; Luhman et al. 1998, 2003; Malhotra 2001) revealed a deficit in the [C II] line strength compared to the far-infrared emission for lower luminosity galaxies. For galaxies with $L_{FIR} < 10^{11} L_\odot$, the $L_{[C II]}/L_{FIR}$ ratio is constant at ∼1%; however, at $L_{FIR} > 10^{11} L_\odot$, the $L_{[C II]}/L_{FIR}$ ratio decreases to ∼0.1%–0.01%. This decrease is known as the "[C II] deficit," and many attempts have been made over the past two decades to investigate its origin (e.g., Hailey-Dunsheath et al. 2010; Ivison et al. 2010; Stacey et al. 2010; Graciá-Carpio et al. 2011; Valtchanov et al. 2011; Farrah et al. 2013; Gullberg et al. 2015; Lutz et al. 2016; Díaz-Santos et al. 2017).

Among the various explanations proposed for this behavior are: [C II] self-absorption, strong continuum extinction at 158 μm; collisional quenching of [C II] emission; high ionization parameters; and metallicity dependence (see Smith et al. 2017 for an extensive discussion).

By exploring the $L_{[C II]}/L_{FIR}$ ratio as a function of the star formation rate surface density (Σ_{SFR}) in spatially resolved local galaxies in the KINGFISH sample, Smith et al. (2017) identify a declining relation of the $L_{[C II]}/L_{FIR}$ ratio as a function of Σ_{SFR}. The authors suggest that the [C II] deficit is driven by local physical processes of interstellar gas (e.g., [C II] self-absorption, dust extinction, and dust grain charge), not related to the global properties of the galaxies. Another study of spatially resolved local galaxies in the GOALS sample, by Díaz-Santos et al. (2017), likewise suggest that local processes are the cause of the [C II] deficit; they propose that the radiation field strength to gas density ratio is the driver.

In this paper, we present high-resolution (0."03) ALMA Cycle 3 Band 7 observations of four SMGs at $z \sim 4.4$–4.8, mapping their structure in dust and [C II] emission on ∼200 pc scales. Our observations show a range of morphologies in the observed 345 GHz dust continuum emission (rest-frame 160 μm) and [C II] emission lines. In Section 3, we describe the observations and data reduction. In Section 4, we present our analysis. Sections 5 and 6 provide our discussion and conclusions. We assume a cosmology with $\Omega_\Lambda = 0.73$, $\Omega_m = 0.27$ and $H_0 = 72$ km s^{-1} Mpc^{-1}, in which 1″ corresponds to a physical scale of 6.7 kpc at $z \sim 4.4$.

2. Sample

Three of our targets (ALESS 61.1, ALESS 65.1, and ALESS 73.1) were selected from ALMA Band 7 (observed 870 μm/345 GHz) follow-up observations of sources detected in the single-dish LABOCA Extended *Chandra* Deep Field South Submm Survey (LESS, Weiß et al. 2009). The ALMA Cycle 0 continuum observations of these SMGs were reported in Hodge et al. (2013) (see Table 1) and revealed serendipitous detections of [C II] in ALESS 61.1 and ALESS 65.1, establishing the redshifts as $z = 4.4189$ and $z = 4.4445$, respectively (Swinbank et al. 2012). The redshift of ALESS 73.1 was already known ($z = 4.756$) and is also detected in [C II] emission from ALMA Cycle 0 observation (Coppin et al. 2009; De Breuck et al. 2014).

In addition to the three ALESS sources, we include UDS 47.0[19] from the ALMA follow-up program of the SCUBA-2 Cosmology Legacy Survey (Geach et al. 2017). A pilot study observed the 30 brightest SCUBA-2 sources in the ∼1 deg^2 UKIDSS/UDS field (Simpson et al. 2015a, 2015b, 2017). These 0."3 resolution ALMA observations revealed a serendipitous detection of [C II] emission at 350.78 GHz, establishing the redshift as $z = 4.420$. The now-complete ALMA survey of $\gtrsim$700 submillimeter sources in the UDS field will be reported in S. Stach et al. (2018, in preparation).

2.1. Physical Properties

We determine the far-infrared luminosity of the galaxies in our sample by fitting modified blackbodies to their spectral energy distributions, including (deblended) 250, 350, 500 μm flux densities (see Swinbank et al. 2014). We adopt an average dust temperature of $T_d = 50 \pm 4$ K, a dust emissivity index of

---

[19] The numerical identifier for this SCUBA-2 source from Simpson et al. (2017) changed in the final version of the S2CLS UDS catalog (Geach et al. 2017) with the source corresponding to UDS0051 in that work. This ALMA identified SMG is cataloged as AS2UDS0051.0 in S. Stach et al. (2018, in preparation)

Table 1
Source Properties

Source	z	R.A.	Decl.	Discovery Resolution	$S_{345\ \mathrm{GHz}}$	$SdV_{[\mathrm{C\,II}]}$	$\mathrm{FWHM}_{[\mathrm{CII}]}$	L_{FIR}
		(J2000)			(mJy)	(Jy km s^{-1})	(km s^{-1})	($10^{12}\,L_\odot$)
ALESS 61.1	4.4189 ± 0.0004 (a)	03:32:45.88	-28:00:23.4	$1\farcs8 \times 1\farcs2$	4.3 ± 0.5	2.5 ± 0.4	230 ± 25	3.1 ± 0.2
ALESS 65.1	4.4445 ± 0.0005 (a)	03:32:52.25	-27:35:26.2	$1\farcs8 \times 1\farcs2$	4.2 ± 0.4	5.4 ± 0.7	490 ± 35	3.1 ± 0.2
ALESS 73.1	4.7555 ± 0.0001 (b)	03:32:29.30	-27:56:19.6	$0\farcs65 \times 0\farcs40$	6.6 ± 0.2	7.4 ± 0.4	375 ± 105	2.9 ± 0.2
UDS 47.0*	4.4201 ± 0.0001 (c)	02:19:24.85	-05:09:20.8	$0\farcs35 \times 0\farcs25$	8.7 ± 0.6	4.3 ± 0.9	935 ± 250	3.2 ± 0.4

Note. The asterisk indicates that UDS 47.0 from Simpson et al. (2017) has since changed name to AS2UDS0051.0 in S. Stach et al. (2018, in preparation). Column 1: Source Names. Column 2: spectroscopic redshift from the observed [C II] frequency, (a) Swinbank et al. (2012), (b) De Breuck et al. (2014), and (c) this work. Columns 3 and 4: source positions. Column 5: resolution of the observations from ALMA Cycle 0 and 1. Column 6: 345 GHz dust continuum flux density from the lower-resolution ALMA cycle 0 and 1 observations (Swinbank et al. 2012; De Breuck et al. 2014; Simpson et al. 2015a). Column 7: velocity-integrated line flux of the [C II] emission lines detected in ALMA Cycle 0 and 1 (Swinbank et al. 2012; De Breuck et al. 2014). Column 8: FWHM of the [C II] emission lines detected in ALMA Cycle 0 and 1 (Swinbank et al. 2012; De Breuck et al. 2014). Column 9: infrared luminosity determined by assuming $T_\mathrm{d} = 50$ K, as determined for 13 $z \sim 4.4$ [C II] identified SMGs in the UDS (E. Cooke et al. 2018, in preparation).

$\beta = 1.5$, and assume the dust is optically thick at $\lambda = 70\,\mu$m. The choice of dust temperature is motivated by recent studies by Faisst et al. (2017) and E. Cooke et al. (2018, in preparation), both of which suggest that high-redshift galaxies with high specific star formation rates have higher characteristic dust temperatures than redshift $z \sim 2$ SMGs ($T_\mathrm{d} \sim 35$ K e.g., Chapman et al. 2005; Swinbank et al. 2012; Weiß et al. 2013). E. Cooke et al. (2018, in preparation) stack *Herschel* PACS and SPIRE photometry (including from 100, 160, 250, 350, 500 μm) and ALMA 870 μm continuum measurements of thirteen $z \sim 4.5$ ALMA SMGs with similar selection criteria to our sample, and thereby show that the ALMA SMGs at redshift $z \sim 4.4$ have characteristic dust temperatures of $T_\mathrm{d} = 50 \pm 4$ K. We note that the far-infrared luminosity is sensitive to the dust temperature, where a lower dust temperature will result in a lower far-infrared luminosity. In Table 1, we provide the far-infrared luminosities from from the best-fit modified blackbodies.

We calculate the dust masses using the measured continuum flux from ALMA listed in 1 and $M_\mathrm{d} = S_\nu D_\mathrm{L}^2 / (\kappa B_\nu(T_\mathrm{d})(1 + z))$, where $\kappa B_\nu(T_\mathrm{d})$ is the Planck function modified by the dust-absorption coefficient of $0.076\,\mathrm{m^2\,kg^{-1}}$ (James et al. 2002), which has been corrected from the rest-frame wavelength of $\sim 160\,\mu$m to observed wavelength of $\sim 870\,\mu$m, assuming $\beta = 1.5$, D_L is the luminosity distance and S_ν is the observed flux density at frequency ν. We adopt a characteristic dust temperature of 50 K and $\beta = 1.5$ (Table 3). Here, we only use a single modified blackbody; however, the dust mass for ALESS 73.1 was determined by Swinbank et al. (2014) to be $9.3 \pm 0.6 \times 10^8\,M_\odot$ for a multi-component model. This difference in masses is likely due to the different dust temperatures and assumed β-values, combined with the fact that the multi-component model traces a larger fraction of the dust mass at multiple temperatures. None of the other three SMGs have previously derived dust masses.

Adopting a single gas-to-dust mass ratio of $\delta_\mathrm{GDR} = 90 \pm 25$ (Swinbank et al. 2014), we estimate the gas masses (Table 3). Also listed in Table 3 are gas masses estimated using the [C II] luminosities and the scaling relation: $M_\mathrm{gas} = 10 \pm 2 \times (L_{[\mathrm{C\,II}]}/L_\odot)$ (Swinbank et al. 2012). The two independent methods of estimating the gas masses result in masses agreeing within the uncertainties.

3. Observations and Reduction

The four SMGs in our sample were observed with ALMA in Band 7 on 2015 November 9–14 for 22.7 to 40.7 minutes on source, using 44–47 antenna in extended configurations, with the longest baselines being ~ 16.2 km (2015.1.00456.S). The receivers were tuned such that one of the two spectral windows in the 7.5 GHz side-band was centered to cover the expected frequency of the [C II] emission line. The FWHM of the ALMA primary beam is $18''$ at 345 GHz. For the three ALESS sources, the QSOs J0522$-$3627, J0334$-$4008, and J0348$-$2749 were used as bandpass, flux, and phase calibrator, while the QSOs J0238+1636 and J0217$-$0820 were used for UDS 47.0.

We used the Common Astronomy Software Application (McMullin et al. 2007, CASA) version 4.5.3 to reduce the data for all four sources and version 4.6.0 for further analysis. The ALMA pipeline was used for the reduction and delivered a high-quality product adopted for the analysis without further modifications. The data were imaged using the CLEAN algorithm in CASA, with natural weighting (ROBUST = 2), in order to recover as much of the extended emission as possible. We CLEAN the images to the rms level of 27–47 μJy beam^{-1} (see Table 2). Using natural weighting and the full available uv-coverage results in a synthesized beam size of $0\farcs03 \times 0\farcs02$ at position angle (P.A.) of 50°–59° for all four SMGs. We created maps at intermediate resolution by applying an outer uv-taper of 3500 kλ to the data when imaging. This results in a synthesized beam size of $0\farcs05 \times 0\farcs04$ at P.A. of 51–59° and an rms of 35–60 μJy beam^{-1}. Finally, we create our lowest resolution ($0\farcs22 \times 0\farcs18$) maps with rms of 0.2–0.3 mJy beam^{-1} by applying an outer uv-taper of 350 kλ to the data when imaging.

We note that the observations were taken in ALMA's most extended configuration, which resulted in a well-covered uv-plane for baselines $\gtrsim 250$ kλ, but poorer coverage at short baselines equivalent to the largest angular resolution (LAS) of $\sim 0\farcs42$. This means that low surface-brightness emission, normally traced by shorter baselines (i.e., lower resolution) is difficult to detect. As we will show, the dust continuum sizes of our sources are $\lesssim$LAS, and so we recover most of the flux in the naturally weighted maps. However, the [C II] emission from these sources appear more extended, and so our high-resolution observations resolve out most of the emission. This can result in an incomplete picture of the morphology and extent of the

Table 2
Continuum Properties of Our Sample at Natural Weighting (0″03) and Intermediate (0″2) Resolution

Source	Natural Weighting (0″03)				Low-resolution (0″2)				Sizes	
	rms (μJy beam^{-1})	S/N	S (mJy)	Recovered Flux	rms (μJy beam^{-1})	S/N	S (mJy)	Recovered Flux	FWHM^{uv} (arcsec)	Aperture (arcsec)
ALESS 61.1	42	7.4	3.5 ± 0.3	$81 \pm 12\%$	0.32	7.7	6.5 ± 0.2	$150 \pm 20\%$	0.33 ± 0.04	0.40
ALESS 65.1	42	7.5	3.0 ± 0.2	$71 \pm 10\%$	0.22	9.8	4.8 ± 0.2	$110 \pm 10\%$	0.30 ± 0.04	0.30
ALESS 73.1	27	8.3	2.9 ± 0.2	$44 \pm 3\%$	0.16	11.7	5.4 ± 0.2	$80 \pm 5\%$	0.43 ± 0.03	0.36
UDS 47.0	47	6.6	5.6 ± 0.3	$64 \pm 8\%$	0.25	20.8	10.2 ± 0.2	$120 \pm 10\%$	0.30 ± 0.02	0.30

Note. Column 5: percentage of recovered flux from ALMA cycle 0/1 data (Swinbank et al. 2012; De Breuck et al. 2014; Simpson et al. 2015a). Column 9: percentage of recovered flux from ALMA cycle 0/1 data (Swinbank et al. 2012; De Breuck et al. 2014; Simpson et al. 2015a). Column 10: FWHM given by the Gaussian profile fit to the amplitude as a function of uv-distance. Column 11: optimized aperture size.

system; therefore, such high-resolution data must be interpreted with care.

4. Analysis

The resolution of the naturally weighted maps (i.e., 0″03) enables us to search for sub-structures in these sources on ∼200 pc scales. Figure 1 shows the 345 GHz continuum maps at this resolution, which reveal a broad range of apparent morphologies: smooth and compact sources in ALESS 61.1, ALESS 65.1 and ALESS 73.1, and extended structure that appears to break up into ∼200 pc scale clumps in UDS 47.0.

The peaks of the 345 GHz continuum for the four sources are detected at 7.4–8.3σ, with an optimized aperture size determined by using a curve of growth we recover between 44 ± 3 and $81 \pm 12\%$ of the integrated flux density measured from the low-resolution ALMA Cycle 0/1 observations (Swinbank et al. 2012; De Breuck et al. 2014; Simpson et al. 2015a). This suggests that our maps are missing a fraction of the emission from the most extended low surface brightness dust on scales $\gtrsim 200$ kpc.

To try to recover more of the extended emission in our maps, we also applied an outer uv-taper to the data, thereby giving a greater weight to the shortest baselines—at the cost of reduced resolution. The middle row of Figure 1 shows the intermediate-resolution continuum maps with an outer uv-taper of 3500 kλ at a resolution of ∼300 pc. These maps show more of the extended lower surface brightness emission and have a higher signal-to-noise ratio than the naturally weighted maps. We therefore fit exponential profiles to these maps and find mean Sérsic indices of $n = 1.1 \pm 0.1$, which is in agreement with the indices from ∼0″15 resolution imaging of 16 ALESS SMGs (Hodge et al. 2016).

To maximize the recovered flux, we applied an outer uv-taper of 350 kλ, resulting in our lowest-resolution maps of ∼1.3 kpc (see bottom row of Figure 1), which recover 80%–100% of the continuum flux detected in the ALMA Cycle 0/1 observations (Swinbank et al. 2012; De Breuck et al. 2014; Simpson et al. 2015a, see Table 2). It is only for ALESS 73.1 that there is an indication that we are still resolving out some flux in these low-resolution maps, where we recover $80 \pm 5\%$ of the flux detected in ALMA Cycle 0/1. In later calculations, we treat the flux recovered from our low-resolution data as the total flux.

4.1. [C II] Emission Lines

Lower-resolution ALMA studies have demonstrated that these four SMGs are all bright [C II] emitters (Swinbank

et al. 2012; De Breuck et al. 2014). By using uv-tapering, we recovered 80%–100% of the continuum flux detected in ALMA cycle 0/1. However, uv-tapering recovers emission only in the image plane, and does not improve the signal-to-noise ratio of the spectral line. Therefore, we search for [C II] emission in our 0″03 observations and select extraction apertures to maximize the recovered signal-to-noise ratio of the line emission. This results in the recovery of modest, significant (2.7–4.7σ) [C II] emission lines (see Figure 2), with measured rms values for the spectra of 2.0–7.4 mJy in 130–210 km s^{-1} channels (see Table 4). Figure 2 shows the moment-zero maps with a uv-taper of 500 kλ (0″17 × 0″16) and compares the recovered [C II] emission to the spectra from the lower-resolution observations from ALMA Cycles 0 and 1 (Swinbank et al. 2012; De Breuck et al. 2014).

ALESS 61.1 and ALESS 65.1 were detected in [C II] emission in ALMA Cycle 0; we recover between 90 and 100% of the velocity integrated line flux at 0″03 resolution, using apertures with diameters of 0″6 and 0″72 respectively.
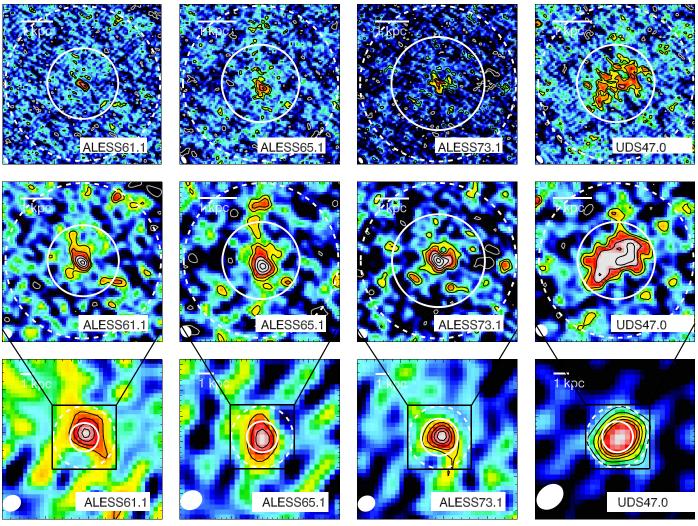
For ALESS 73.1 at 0″03 resolution (Figure 2), our observations recover only ∼20% of the peak flux emission in the 0″5 resolution map from De Breuck et al. (2014). To compare with the emission line profiles detected in the 0″5 resolution data (De Breuck et al. 2014), we simply scale the peak of the 0″5 resolution [C II] line to that of the 0″03 emission line (i.e., multiply by 0.2). This results in the red wing of the [C II] emission line we detect being consistent with the red wing of the [C II] emission line from the 0″5 resolution data before downscaling.

Emission from [C II] was detected for UDS 47.0 as a very broad line at ∼351 GHz in the shallower 0″3 data from ALMA Cycle 1 (Simpson et al. 2015b, 2017). In our deeper 0″03 resolution observations, we detect a broad ∼4σ [C II] emission line. Adopting an optimized aperture size of 0″6, we recover the full flux seen in the shallower low-resolution observations from ALMA Cycle 1.

4.2. Size Estimates from uv-plane Fits

4.2.1. Continuum

The natural-weighted resolution 345 GHz dust continuum maps recover between 44% and 81% of the continuum flux detected at lower resolution. This suggests that around $40 \pm 20\%$ of the flux has been resolved out at 0″03 resolution, compared to the Cycle 0/1 maps. To estimate the size of the rest frame 160 μm emission in the SMGs, we determine the behavior of the amplitude as a function of uv-distance. We do this by first aligning the phase center of our cubes with the

Figure 1. Continuum maps at three different resolutions for our sample of SMGs. The white solid and white dashed circles indicate the sizes estimated for the 345 GHz dust continuum emission and the [C II] emitting gas, respectively (see Tables 2 and 4). Top row: naturally weighted (0."03, ~200 pc) 345 GHz continuum maps. The contours are −2σ (white contours) and 2σ, 3σ, and 5σ (black contours). The maps show the continuum morphologies to be either compact and smooth (ALESS 61.1, ALESS 65.1 and ALESS 73.1) or break up into apparent substructures on ~200 pc scales (UDS 47.0). These 0."03 resolution observations recover between 44% and 81% of the continuum flux detected at lower resolution in ALMA Cycle 0/1 (Swinbank et al. 2012; De Breuck et al. 2014; Simpson et al. 2015a). Middle row: intermediate-resolution 345 GHz continuum maps uv-tapered to 0."05 (~300 pc), showing the morphologies of the more extended emission in these sources. The gray contours are −2σ, whereas 2σ, 3σ, 5σ, 7σ, and 9σ are shown as black contours. The lower-resolution images reveal more smooth structures. Bottom row: lowest-resolution 345 GHz continuum maps uv-tapered to 0."2 (~1.3 kpc) resolution, showing the most extended emission observable at this configuration. At this resolution, the SMGs are unresolved and we recover between 80% and 100% of the continuum emission.

source position listed in Table 1. We then radially average the data in 75 kλ bins to extract the amplitudes as a function of uv-separation. For the continuum, a binning of 75 kλ is the most optimal to minimize the scatter; however, the overall trend of the amplitude as a function of uv-distance is independent of the binning. Figure 3 shows the amplitude as a function of the uv-distance for the inner 1500 kλ in each of the four SMGs.

For a point source, the observed amplitudes will be constant as a function of uv-distance, whereas the amplitude declines at larger uv-distances for an extended source. Hence, the physical size of the source can be determined from the FWHM of a half-Gaussian profile fit to these uv-profiles. In that case, the total flux is represented by the peak value of the half-Gaussian fit. As Figure 3 shows, the amplitude declines as a function of uv-distance for the continuum emission in all four SMGs, and they are therefore consistent with a centrally peaked brightness profile, meaning that the sources are resolved. We add the low-resolution observations from Cycle 0/1 to the plots at the

uv-distance corresponding to the LAS of the observations and the single dish flux at 0 kλ, as these represent our best estimate of the total integrated flux. We fit a half-Gaussian profile plus a constant (representing a point source) to the amplitudes, in order to measure the physical size of the emission and establish whether a point source is present. The fitted FWHMs converted into physical sizes are listed in Table 2.

We find that the continuum point source components of the fits are non-zero for all four sources, with flux densities of 0.4–0.7 mJy. This suggests that, on average, about ~14% of the total continuum flux in each source is emitted from a component with a size ≲200 pc.

There is a published size for the 330 GHz continuum, reported for ALESS 73.1 of 0."29 ± 0."06 (De Breuck et al. 2014). To compare with this, we derive a size from a single Gaussian fit without a point source of 0."38 ± 0."05, which is consistent.
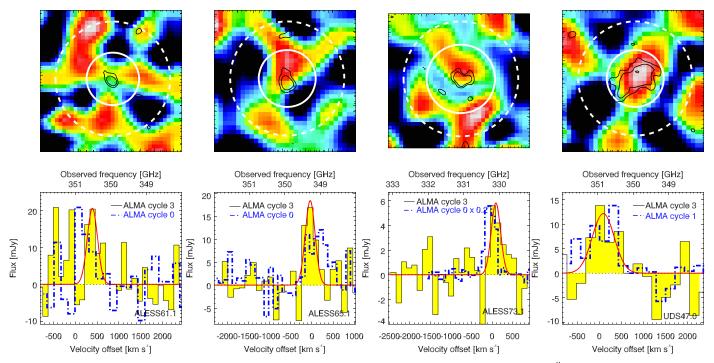
Figure 2. [C II] moment-zero maps and comparison of the continuum-subtracted [C II] emission-line spectra from the new 0″.03 resolution data and the lower-resolution (see Table 1) ALMA Cycle 0/1 observations. The moment-zero [C II] are obtained using a *uv*-taper of 500 kλ. Overlaid in white solid and white dashed circles are the *uv*-derived sizes estimated for the 345 GHz dust continuum emission and the [C II] emitting gas, respectively (see Tables 2 and 4). The spectra from the 0″.03 resolution observations have been binned up to 130–210 km s^{-1} per channel. Only by using large, optimized apertures (compared to the resolution) do we recover the [C II] flux seen in the shallower Cycle 0/1 observations with large uncertainties. This indicates that the [C II] emission is very extended and relatively smooth in these sources, and hence our 0″.03 resolution observations are resolving out the bulk of the extended [C II] flux emission in these sources. The ALMA Cycle 0 spectrum for ALESS 73.1 from De Breuck et al. (2014) has been scaled down by a factor of five. The line peak on our Cycle 3 observations of ALESS 61.1 is shifted by ∼400 km s^{-1} and is dominated by high noise spikes on the blue side of the line. The shift in line center seen in the other sources may be due to low signal-to-noise ratio or the fact that the small-scale structure detected in our high-resolution observations is not uniformly distributed within the sources.

As already stated, we only recover the total continuum flux density from the low-resolution observations in the *uv*-tapered map by applying an outer taper of ∼350 kλ. Figure 3 illustrates that, because the amplitudes only diverge from the constant value of 0.4–0.7 mJy at *uv*-distances of ≲350 kλ, only a strong *uv*-taper gives enough weight to the shortest baselines to lower the resolution sufficiently to make a significant difference in the recovered flux density.

4.2.2. [C II] Emission

We recover [C II] emission lines in all four SMGs, but only at low significance (2.7–4.7σ). To determine whether the [C II] emission is resolved and estimate its extent, we extract the amplitude as a function of the *uv*-distance for the spectral channels spanning the [C II] emission. We align the phase center to the same position as for the continuum, and fit a zero-order polynomial in the *uv*-plane to the line-free channels to determine the continuum level. We then subtract the fitted continuum in the *uv*-plane and extract the amplitude as a function of *uv*-distance for the spectral channels spanning the [C II] emission. Estimates of the physical extent of the [C II] emission use the same method as for the continuum, i.e., by fitting a half-Gaussian profile plus a point source component to the amplitude as a function of the *uv*-distance, and then converting the fitted FWHMs of the Gaussian profile to arcseconds. Figure 3 shows the profiles of the continuum emission and the [C II] emission, with the FWHMs given in Table 4. Note that, apart from the poor sampling of the inner part of the *uv*-plane, the visibilities for the [C II] data are derived from

only a limited spectral range; and thus contain fewer data points. We therefore apply a larger binning of 300 kλ for ALESS 61.1 and UDS 47.0 and 75 kλ for ALESS 65.1 and ALESS 73.1. De Breuck et al. (2014) measure the [C II] emission to have a FWHM of ∼0″.64 in ALESS 73.1, which is consistent with our measurements (FWHM = 0″.7 ± 0″.1).

Our data are not sampled well enough to establish whether unresolved [C II] emitting components are present in these four SMGs. The lower sampling of visibility points in the [C II] data also means that the measured sizes are more uncertain than those for the 345 GHz continuum. We include the lower-resolution observations from Cycle 0/1 in our fits, yielding estimated FWHMs of 0″.3–1″.1 that are comparable to or larger than the LAS of ∼0″.4 recoverable at the antenna configuration of our Cycle 3 observations.

5. Discussion

5.1. Continuum and [C II] Sizes

From the half-Gaussian profile fits in Figure 3, we measure the median continuum size to be 0″.32 ± 0″.03 and the [C II] size to be 0″.65 ± 0″.15 (see Tables 2 and 4). The measured size ratio for our sample suggest that, on average, the [C II] emitting gas is 2.1 ± 0.4 times more extended than the continuum emitting dust. The fact that the continuum sizes are smaller than the LAS allows us to recover between 80 to 100% of the flux detected in ALMA cycle 0/1. The [C II] sizes, however, are larger than the LAS, meaning it is not possible to recover the emission distributed on scales larger than the LAS.
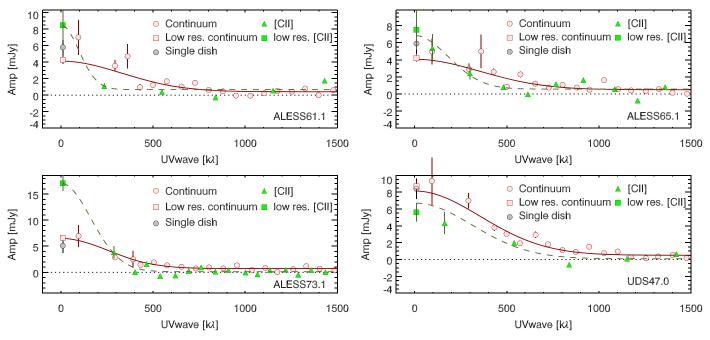
Figure 3. Visibility amplitudes as a function of the *uv*-distance for all four SMGs in the sample for the 345 GHz dust continuum and [C II] emission. The amplitudes for the continuum are extracted by radially averaging the visibilities in 75 kλ bins over the full frequency range. For the [C II] emission in ALESS 61.1 and UDS 47.0, a larger binning of 300 kλ had to be applied for the radially averaging of the visibilities, while a binning of 75 kλ was applied to ALESS 65.1 and ALESS 73.1. Here, the line visibilities cover the observed spectral range of the [C II] emission of 350–352 GHz for ALESS 61.1 and UDS 47.0, 348–350 GHz for ALESS 65.1, and 329–311 GHz for ALESS 73.1. The *uv*-coverage is better sampled at long baselines than on shorter ones for our ALMA configuration. The half-Gaussian fits to the continuum emission are overlaid in red, and the half-Gaussian fits to the [C II] emission are shown in green. We also plot the fluxes determined from the lower-resolution data from ALMA Cycle 0 and 1. The 345 GHz dust continuum and [C II] emission of the SMGs are resolved in our observations and the 345 GHz dust continuum sizes of the sources are listed in Table 2 and 4. Despite the sparse *uv*-coverage at <250 kλ, it is evident that the extent of [C II] emission is greater than or equal to the extent of the 345 GHz dust continuum emission in all four SMGs.

This results in low signal-to-noise [C II] emission lines and low-significance moment-zero maps (Figure 2).

Figure 4 compares our estimated [C II] and rest-frame 160 μm continuum sizes for our SMGs. It also shows the [C II] and rest-frame 160 μm dust continuum sizes for four quasars at $z = 4.6$–7.1 (Wang et al. 2013; Kimball et al. 2015; Díaz-Santos et al. 2016; Venemans et al. 2017), a starburst galaxy at $z = 3.4$ (Nesvadba et al. 2016), a Lyα Blob at $z = 3.1$ (Umehata et al. 2017), and LBGs at $z = 5.3$–6.1 (Capak et al. 2015; Jones et al. 2017). The [C II] and rest-frame 160 μm dust continuum observations have been taken at the same spatial resolution in each source, but this varies between $0\rlap.{''}2$ and $1''$. These observations appear to support the conclusion that [C II] emitting components are more extended than the rest-frame 160 μm dust components in a majority of the systems.

Although the resolution of these studies is ~6–30 times lower than our observations, the relative sizes of the [C II] and rest-frame 160 μm dust emission still suggest that the [C II] emitting gas is more extended than the rest-frame 160 μm continuum. The weighted mean of the [C II] to rest-frame 160 μm dust continuum size, including our four SMGs and the comparison sample, is 1.6 ± 0.4. Only three of the 18 galaxies have apparently larger rest-frame 160 μm continuum than [C II] sizes and therefore lie off this relation. Of these, only one is significantly different: a lensed starburst galaxy, where the relative sizes are sensitive to the details of the lens model. The fact that the majority of the galaxies follow a trend, although they are very different populations with different gas masses and active galactic nucleus (AGN) luminosities, suggests that these global physical parameters are unlikely to account for the
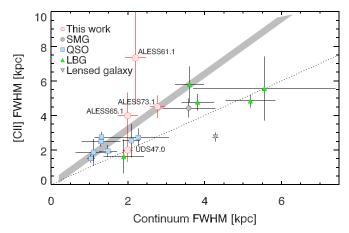

Figure 4. Spatial FWHM of the rest-frame 160 μm continuum emission versus the FWHM of the [C II] emission for the four SMGs in this work, along with high-redshift $(3.1 < z < 7.1)$ galaxies in the literature that have similar measurements (Wang et al. 2013; Capak et al. 2015; Kimball et al. 2015; Díaz-Santos et al. 2016; Nesvadba et al. 2016; Jones et al. 2017; Umehata et al. 2017; Venemans et al. 2017). We see that the [C II] emitting gas is more extended than the rest frame 160 μm emitting dust, for the majority of the galaxies. The dotted line is the 1:1 relation, while the gray-shaded region shows the weighted mean of the [C II] to continuum size of 1.6 ± 0.4.

observed size differences. This means that the nature of the dominant heating source (whether, for example, it is AGN or starburst activity) does not appear to significantly influence the relative size of the rest-frame 160 μm dust continuum and [C II] emitting gas.

At these high redshifts $(z \simeq 4.5)$, the temperature of the cosmic microwave background (CMB) is $\simeq 15$ K. This means that, if the star-forming dust has similar temperature to the

Table 3
Dust and Gas Masses

Source name	$M_{\rm dust}$ $[10^8\,M_\odot]$	$M_{\rm gas}$ $[10^{10}\,M_\odot]$	$M_{\rm gas}^{\rm [C\,II]}$ $[10^{10}\,M_\odot]$
ALESS 61.1	2.9 ± 0.6	2.6 ± 0.9	1.5 ± 0.4
ALESS 65.1	2.8 ± 0.6	2.6 ± 0.9	3.2 ± 0.8
ALESS 73.1	4.3 ± 0.8	3.9 ± 1.3	4.9 ± 1.0
UDS 47.0	5.9 ± 1.1	5.3 ± 1.8	2.6 ± 0.7

Note. The estimated dust and gas masses based on the ALMA Cycle 0/1 observed 345 GHz dust continuum, extrapolated to rest-frame assuming $\beta = 1.5$ and [CII] fluxes. The dust masses ($M_{\rm dust}$) are calculated using the 345 GHz continuum flux, which are then scaled using a gas-to-dust mass ratio of 90 ± 25 to achieve the gas masses ($M_{\rm gas}$). Gas masses estimated using the [C II] fluxes ($M_{\rm gas}^{\rm [C\,II]}$) are likewise listed, and agree with the gas masses estimated using the dust mass.

CMB, it will not be detectable (da Cunha et al. 2013; Zhang et al. 2016). We note that, given that the dust temperature is higher than the background CMB, this means that the CMB is unlikely to be the reason why the [C II] emission is 1.6 times more extended than the rest-frame 160 μm dust emission.

5.2. Velocity Gradients and Dynamical Masses

The [C II] emission line is one of the brightest cooling lines of the interstellar medium and traces the ionized, neutral, and molecular gas. It is therefore a good tracer of the gas dynamics in high-redshift galaxies (e.g., Carniani et al. 2013; Capak et al. 2015). Only ALESS 73.1 and UDS 47.0 have low-resolution observations from Cycle 0/1 deep enough to allow us to search for possible velocity gradients. From the study of De Breuck et al. (2014), it is already known that the gas in ALESS 73.1 has a rotating configuration, and the broad line of UDS 47.0 suggests that a velocity gradient may also be present there.

To investigate the velocity gradient in these two SMGs, we make moment-zero maps (i.e., narrow-band images) in the low-resolution (from ALMA Cycle 0/1, see Table 1) continuum-subtracted cube of the channels covering the [C II] emission. We make two independent maps; one of the redshifted half of the line and the other of the blueshifted half. These cover $\pm 400\,{\rm km\,s^{-1}}$ for UDS 47.0 and $\pm 200\,{\rm km\,s^{-1}}$ for ALESS 73.1. We find that the peak of the [C II] emission shifts by $0\farcs25 \pm 0\farcs04$ (~1.7 ± 0.3 kpc) between the red and blue halves of the line for UDS 47.0 and $0\farcs24 \pm 0\farcs01$ (~1.5 ± 06 kpc) for ALESS 73.1. This implies a velocity gradient across the [C II] emitting gas in both SMGs.

Having established the presence of a velocity gradient, and using a disk model for the dynamics, we estimate the dynamical masses ($M_{\rm dyn}\sin(i) = R \times v^2/G$) of ALESS 73.1 and UDS 47.0 within a region given by twice the size of the [C II] sizes listed in Table 2 corresponding to $R = 5$ kpc and $R = 4$ kpc for ALESS 73.1 and UDS 47.0, respectively. Using the line widths of the [C II] lines detected in ALMA Cycle 0/1 (see Table 1), this yields dynamical masses of $3.7 \pm 0.7 \times 10^{10} \sin(i)\,M_\odot$ for ALESS 73.1 and $20 \pm 4 \times 10^{10} \sin(i)\,M_\odot$ for UDS 47.0. Using a similar disk model, De Breuck et al. (2014) estimate an inclination angle of $i = 50° \pm 8$ for ALESS 73.1, which is similar to the average inclination angle calculated by Law et al. (2009). By assuming the same inclination angle for UDS 47.0 and the

gas masses listed in Table 3, we estimate an average gas mass fraction within the half-mass radii assumed to calculate the dynamical masses of 0.4 ± 0.2. This is in agreement with the result from Tacconi et al. (2018) for redshift $\lesssim 4$ star-forming galaxies when converting to the same units.
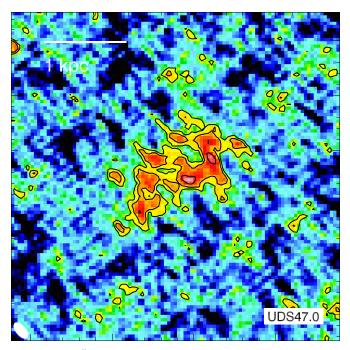
5.3. Morphologies

Figure 1 demonstrates that three SMGs in our sample (ALESS 61.1, ALESS 65.1, and ALESS 73.1) show smooth 345 GHz dust continuum morphology, while one (UDS 47.0) appears to have structure. However, the apparent structures seen for UDS 47.0 have significance levels of just 3.9–5.4σ. Similarly, a recent high-resolution (0$\farcs$03) resolution 345 GHz dust continuum study by Iono et al. (2016) of three $z \sim 4.3$ AzTEC SMGs claimed to reveal about $40 \geqslant 3\sigma$ 200 pc clumps. These visually identified structures are similar to the features we see in UDS 47.0.

To test whether the structures in UDS 47.0 are likely to be real, or if they could arise from noise in smooth disk light profiles, we model a set of observations of smooth profiles. We use the CASA tasks SIMOBSERVATIONS and SIMANALYSIS to create a library of simulated interferometry observations of exponential disks as they would appear if observed with ALMA in the same configuration as used for our observations and with similar noise properties (following the example of Hodge et al. 2016). Our 50 input models of smooth exponential disk models have Sérsic indices of $n = 1$ (comparable to what we see in our sample) and flux densities and sizes of 8.7 ± 0.6 mJy and $0\farcs28 \pm 0\farcs03$, as seen for UDS 47.0 (Simpson et al. 2015a). The results of these simulations also reveal apparently clump-like structures (Figure 5). While these structures qualitatively look similar to those seen in UDS 47.0, we attempt to quantitatively compare the flux distribution between the simulated maps and the observed map for UDS 47.0. We do this by fitting single smooth profiles (with the Sérsic index as a free parameter, to the simulated maps), and subtracting the best fit model. For the central part of the residual image, the number of pixels as a function of the flux has a Gaussian profile with a tail of excess emission at positive values. This excess flux should represent the emission seen in possible structures, and we isolate it by subtracting a one-dimensional Gaussian profile fit to the histogram.

We apply this analysis to both the simulated smooth disks and the observation of UDS 47.0. A Kolmogorov–Smirnov test comparing the average of the residual pixel distribution from the simulated smooth disks to that of the observations reveals that the likelihood of the observed map being drawn from the simulated library of smooth disks is ~70%. Applying the same analysis to the three other SMGs in our sample shows that they are consistent with smooth morphologies.

Our simulated library of smooth disks, in combination with the apparently smooth morphology of three out of four SMGs in our sample, illustrates that smooth disks can appear to have substructures when observed at high resolution and with sparse coverage of the inner part of the uv-plane. We conclude that it is not possible to rule out the hypothesis that all four SMGs in our sample are smooth exponential disks.

We note that the structures identified by Iono et al. (2016) in their sources have similar significances to those seen in UDS 47.0. Moreover, only ~30% of the continuum flux detected at 0$\farcs$7 resolution with the SMA (Younger et al. 2008; Iono et al. 2016) has been recovered in their 0$\farcs$03 ALMA

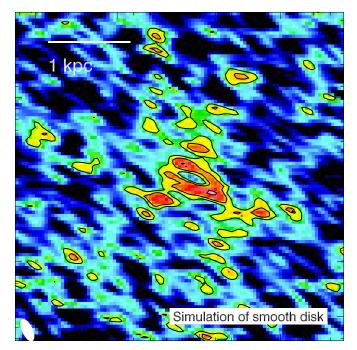**Figure 5.** Left: 0″03 resolution 345 GHz continuum map of UDS 47.0, showing apparent clumps with sizes comparable to the synthesized beam (∼200 pc). Right: example of a simulated 345 GHz continuum map of a smooth exponential disk observed with the same observational parameters as the data shown in the map to the left. Both maps show similar apparent structures, but the right-hand simulated map is known to be a smooth exponential disk. Analysis of the flux distribution of the pixels reveal that there is a 70% probability that the map of UDS 47.0 is drawn from the simulated library of models. It is therefore not possible to rule out the hypothesis that UDS 47.0 is a smooth disk from our observations, and so we suggest that the apparent structures identified by eye may be misleading.

maps, with less than 20% of that in the claimed clumps. The fact that the resolution and depth of the observations in Iono et al. (2016) are similar to our 0″03 maps, and that their claimed structures contain only a small fraction of the total flux, casts doubt on whether their clumps are real structures either.

5.4. Expected Size of Clumps

As noted above, one of the sources in our sample (UDS 47.0) appears to have a clumpy morphology in our high-resolution ALMA continuum maps; however, we have suggested that this is not statistically significant. Nevertheless, we can also ask if we should expect to see sub-structures at this resolution, given the estimated star formation rate surface densities of these galaxies.

The average sizes of star-forming clumps in a self-gravitating gas disk are given by the Jeans length,

$$\lambda_J \approx \frac{\sigma^2}{G\Sigma_{\mathrm{gas}}}, \qquad (1)$$

where G is the gravitational constant, Σ_{gas} is the gas surface density, and σ the velocity dispersion of the gas within a clump (Toomre 1964). We estimate Σ_{gas} using:

$$\left(\frac{\Sigma_{\mathrm{SFR}}}{M_\odot\,\mathrm{yr}^{-1}\,\mathrm{kpc}^{-2}}\right) = A\left(\frac{\Sigma_{\mathrm{gas}}}{M_\odot\,\mathrm{pc}^{-2}}\right)^n, \qquad (2)$$

where $A = 1.5 \times 10^{-4}$ and $n \simeq 1.5$ (Kennicutt 1998; Swinbank et al. 2012). For clumps to have a size of $\gtrsim 200$ pc (and thus be observable at the resolution of our observations at the estimated gas surface density), the velocity dispersions within the gas disk have to be $\sigma \gtrsim 60$ km s^{-1} for ALESS 61.1, which has the lowest estimated gas surface density of our

sample, and $\sigma \gtrsim 85$ km s^{-1} for UDS 47.0, which has the highest gas surface density.

A recent high-resolution (∼0″03) observation of the lensed SMG SDP.81 (ALMA Partnership et al. 2015; Hatsukade et al. 2015) measured the velocity dispersions in regions within the gas disk in this system to be in the range of 11–35 km s^{-1} (Swinbank et al. 2015). The velocity dispersion of the gas disk in ALESS 73.1 was likewise estimated to be 40 ± 10 km s^{-1} (De Breuck et al. 2014). Thus, the required velocity dispersions to observe clumps at 200 pc resolution are 1.5–2 times higher than those observed in other SMGs. Hence, if our sources have velocity dispersions comparable to that observed for other SMGs, then any clumps in their gas disks would have sizes below the resolution limit of our ALMA observations. This suggests that the clumps in UDS 47.0, if real, are unlikely to represent self-gravitating physical structures.

5.5. The [C II] Deficit

We now turn to the overall energetics of these systems and their cooling. As noted earlier, emission from [C II] is a major contributor to the gas cooling, carrying 0.1%–1% of the far-infrared luminosity in luminous starburst galaxies (Stacey et al. 1991; Brauher et al. 2008; Graciá-Carpio et al. 2011). The [C II] to far-infrared luminosity ratio ($L_{[\mathrm{C\,II}]}/L_{\mathrm{FIR}}$) varies with far-infrared luminosity in local galaxies, such that the most far-infrared luminous galaxies have a lower $L_{[\mathrm{C\,II}]}/L_{\mathrm{FIR}}$ ratio. Figure 6 shows $L_{[\mathrm{C\,II}]}/L_{\mathrm{FIR}}$ as function of star formation rate surface density for the low-redshift KINGFISH sample (Kennicutt et al. 2011; Dale et al. 2016; Croxall et al. 2017), the GOALS sample (Díaz-Santos et al. 2013; Lutz et al. 2016), and a high-redshift sample of SMGs (Gullberg et al. 2015; Lutz et al. 2016, typically lensed).
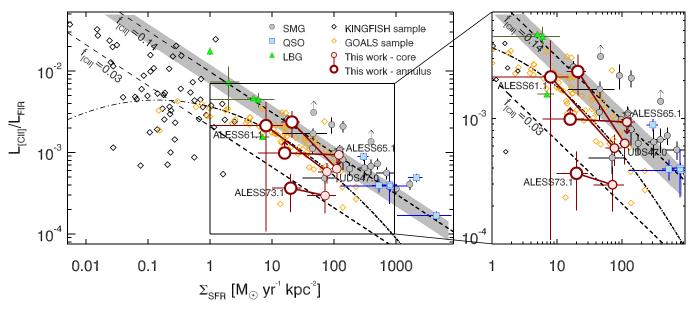
Figure 6. The $L_{[C\,II]}$ to L_{FIR} ratio as a function of the star formation rate density for local galaxies in the KINGFISH and GOALS (Armus et al. 2009; Lutz et al. 2016; Díaz-Santos et al. 2017), a sample of high-redshift galaxies (Wang et al. 2013; Capak et al. 2015; Gullberg et al. 2015; Kimball et al. 2015; Lutz et al. 2016; Nesvadba et al. 2016; Díaz-Santos et al. 2017; Jones et al. 2017; Umehata et al. 2017; Venemans et al. 2017), and our sample of four $z \sim 4.5$ SMGs. We note that the sizes used to achieve the star formation rate densities for the GOALS sample are the 70 μm effective radii under the assumption of a uniform dust temperature. The inner parts of our four galaxies are plotted as red circles and the outer annuli as stars. The respective core and annuli measurements are connected by solid lines. For three SMGs in the sample, the Σ_{SFR} is lower in the outer annulus and the $L_{[C\,II]}/L_{FIR}$ ratios is higher than for the core. This suggests that the [C II] deficit is a local process. The $L_{[C\,II]}/L_{FIR}$ ratio as a function of the FIR surface density and the mass fraction of [C II] compared to the total mass ($f_{[C\,II]}$) from Muñoz & Oh (2016) is plotted as the gray shaded area, assuming $f_{[C\,II]} = 0.10$–0.17, and the curved power law fitted to galaxies in GOALS from (Díaz-Santos et al. 2017) is plotted as the dotted–dashed curve. We note that both the high- and low-redshift samples exhibit a large scatter around the two models. Our data agree with both models, so it is not possible to distinguish which of the two models is closer to the true explanation.

Table 4
Properties of the [C II] Emission Lines Detected at 0″03 Resolution

Source	rms (mJy)	S/N	$SdV_{[C\,II]}$ (Jy km s^{-1})	FWHM$_{[C\,II]}^{line}$ (km s^{-1})	FWHM$_{[C\,II]}^{uv}$ (arcsec)	Aperture (arcsec)	Recovered (%)
ALESS 61.1	7.4	2.7	4.6 ± 1.7	280 ± 110	1.1 ± 0.4	0.72	180 ± 80
ALESS 65.1	4.0	4.7	4.9 ± 1.0	270 ± 70	0.6 ± 0.2	0.6	90 ± 20
ALESS 73.1	2.0	3.0	1.6 ± 0.5	270 ± 110	0.7 ± 0.1	0.72	22 ± 7
UDS 47.0	4.4	3.1	6.8 ± 1.8	590 ± 250	0.3 ± 0.1	0.6	160 ± 50

Note. Column 2: rms of the [C II] spectra. Column 3: signal-to-noise ratio of the [C II] emission lines. Column 4: velocity-integrated line fluxes. Column 5: FWHM of the [C II] line velocity width. Column 6: spatial FWHM given by the Gaussian fit to the amplitude as a function of uv-distance. Column 7: diameter of the aperture used to measure the line flux. Column 8: percentage of recovered line flux.

At the highest star formation rate surface densities (i.e., typically smaller sizes, FWHM $\sim$ 1–3 kpc), we see that the lowest $L_{[C\,II]}/L_{FIR}$ ratios are frequently associated with AGNs, while normal star-forming galaxies (including Lyman Break galaxies) have higher $L_{[C\,II]}/L_{FIR}$ ratios.

We see in Figure 6 that the $L_{[C\,II]}/L_{FIR}$ ratios for our sample agree with the high-redshift comparison sample, but both show a large scatter when compared to the local galaxies from KINGFISH and GOALS. Figure 6 shows that the high-redshift sources generally have higher $L_{[C\,II]}/L_{FIR}$, compared to local galaxies at a fixed far-infrared luminosity.

To investigate if the [C II] deficit is due to a local or global process, we plot two points for each of our SMGs: a core measurement from an aperture the same size as the 345 GHz dust continuum (Table 2); and an annulus the size of the optimized [C II] aperture listed in Table 4. The [C II] luminosities are calculated by extracting two spectra: one within the continuum aperture and one within the [C II] aperture. The [C II] luminosity in the annulus is then given by the difference between the two luminosities. Note that, for

ALESS 65.1, the [C II] emission line is undetected in the core, meaning that the $L_{[C\,II]}/L_{FIR}$ ratio for the core is an upper limit —and therefore a lower limit within the annulus. We scale the far-infrared luminosities and star formation rates according to the fraction of emission we recover within the 345 GHz dust continuum apertures (see Table 2), and assume that the remaining fraction originates from the annulus. The star formation rate surface densities are then calculated using the areas of the continuum apertures for the core measurement and the difference between the [C II] and continuum apertures for the annuli.

We use these measurements to investigate the variations of the $L_{[C\,II]}/L_{FIR}$ ratio within our SMGs. The expanded part of Figure 6 shows the trend between the core measurements and the annuli. All four of the galaxies show the same behavior: the core has lower $L_{[C\,II]}/L_{FIR}$ and higher star formation rate surface density than the surrounding annulus. This follows the relation seen by Smith et al. (2017) for local star-forming galaxies. A higher star formation rate surface density in the

core regions compared with the outer annuli is expected, but the same expectation is not true for the $L_{[C\,II]}/L_{FIR}$ ratio.

The fact that our SMGs follow the same trend seen by, for example, Smith et al. (2017), implies that the [C II] deficit in SMGs is also due to a local process, where the core regions have a higher [C II] deficit than the regions further out from the core.

Smith et al. (2017) suggest that the [C II] deficit is related to the metallicity of the gas, where a low metallicity results in a high $L_{[C\,II]}/L_{FIR}$ ratio. Alternatively, a recent study by Muñoz & Oh (2016) explored the possibility of [C II] saturation. This hypotheses had been proposed before, but had not been investigated in detail (e.g., Stacey et al. 2010; Díaz-Santos et al. 2013; Magdis et al. 2014; Gullberg et al. 2015). Muñoz & Oh (2016) show that the [C II] emission can be thermally saturated at high temperatures. At gas temperatures >92 K (the ground state temperature of [C II]), the [C II] cooling rate becomes constant, forcing the gas to cool through other channels (e.g., the [O I]63 μm fine structure line). This means that the [C II] emission line saturates and a [C II] deficit can therefore occur as a result of the further increase of the far-infrared luminosity. By considering the specific [C II] luminosity (the [C II] luminosity to [C II] mass ratio, $L_{[C\,II]}/M_{[C\,II]}$) and specific far-infrared luminosity (the far-infrared luminosity to gas mass ratio, L_{FIR}/M_{gas}), Muñoz & Oh (2016) predict an $L_{[C\,II]}/L_{FIR}$ relation dependent on the infrared surface density (Σ_{IR}) and fraction of the gas mass in ionized carbon ($f_{[C\,II]} = M_{[C\,II]}/M_{gas}$):

$$\frac{L_{[C\,II]}}{L_{FIR}} \sim 2.2 \times 10^{-3} \frac{f_{[C\,II]}}{0.13} \left(\frac{\Sigma_{IR}}{10^{11} L_\odot\,kpc^{-2}} \right)^{-1/2}. \quad (3)$$

Here, $f_{[C\,II]}$ is estimated to between 0.10 and 0.17, assuming a fixed CO(1–0) to [C II] luminosity ratio, the CO to H_2 conversion factor (α_{CO}), a gas density higher than the critical density of [C II] ($n_{crit} = 2.7 \times 10^3\,cm^{-3}$, e.g., Stacey et al. 2010), and a temperature higher than 92 K. This fraction does not take into account the fact that some of the carbon is in the neutral phase, meaning that the actual mass fraction is likely to be lower. The relation between the [C II] to far-infrared luminosity ratio as a function of the star formation rate surface density found by Muñoz & Oh (2016) adopts fixed values of $G = 100$ and $n_{gas} = 10^4\,cm^{-3}$ for the radiation field strength and the gas density. We plot the predicted trend line on Figure 6 for $f_{[C\,II]} = 0.03$ and 0.14, which span the range of the data, suggesting that fraction of the total mass in ionized carbon is between 3% and 14%.

However, other studies—for example, Díaz-Santos et al. (2017) and Lagache et al. (2018)—argue the [C II] deficit arises from other factors. In particular, they emphasize the importance of a varying radiation field strength to gas density ratio (G/n_{gas}). Díaz-Santos et al. (2017) fit a power law to local ULIRGs from GOALS (see Equation (3) in Díaz-Santos et al. 2017) and find that the suppression of the [C II] to far-infrared luminosity ratio at high far-infrared surface densities could be due to high G/n_{gas} ratios. Using semi-analytical models, Lagache et al. (2018) likewise suggest that the [C II] to far-infrared deficit is correlated with the intensity of the interstellar radiation field. This suggests that the star formation rate surface density is dependent on the geometry of the photon dominated regions and the distribution of the gas and dust within it.

We show the relation between the [C II] to far-infrared luminosity ratio and the star formation rate surface density with $f_{[C\,II]} = 0.10$–0.17 in Figure 6, along with the power-law relation determined by Díaz-Santos et al. (2017). Both the power law from Díaz-Santos et al. (2017) and the model of Muñoz & Oh (2016) are in agreement with our observations. This means that it is not possible, with the existing data, to distinguish between the two models and determine if the [C II] deficit can be explained by a saturation of the [C II] emission at high temperatures and densities in the dense core regions of the SMGs or a high ratio of radiation field strength to gas density. We also note that contributions from other local processes (e.g., [C II] self-absorption, dust extinction, and dust grain charge), may also play a role in the deficit (Smith et al. 2017).

6. Conclusions

We present deep high-resolution (0$\farcs$03) ALMA Band 7 observations of the dust continuum and the redshifted [C II] 158 μm emission line in four SMGs from the ALESS and AS2UDS surveys at $z \sim 4.4$–4.8. These observations resolve the dust and gas distribution on $\sim$200 pc scales and reveal a range of morphologies, ranging from compact and smooth to extended and apparently clumpy.

1. By determining the amplitudes as function of the uv-distance for both the continuum and [C II] emission, we conclude that the [C II] emission is more extended than the rest-frame 160 μm dust continuum emission by a factor of 2.1 ± 0.4. This behavior is also seen in a sample of high-redshift galaxies from the literature, where we find a mean ratio of the [C II] to rest-frame 160 μm dust size of 1.6 ± 0.4.

2. Three of our four SMGs show smooth continuum morphologies at sub-kpc resolution—the fourth, UDS 47.0, appears clumpy at 200 pc resolution. To determine whether the apparent clumps in UDS 47.0 are real, we compare with simulated observations of smooth exponential disks. These comparisons show that smooth morphologies can appear clumpy if observed at high resolution, even in deep observations such as those used here. We conclude that it is not possible to rule out the hypothesis that all of our SMGs are smooth exponential disks. Deeper observations are required to further test this.

3. By comparing the $L_{[C\,II]}/L_{FIR}$ ratio as a function of the star formation rate surface density for the core with a diameter of $\sim$2 kpc of our SMGs to that in the lower-density outskirts, we conclude that the [C II] deficit is likely to be due to local processes, which is in agreement with the conclusion of Smith et al. (2017). Comparing the observed relation between the $L_{[C\,II]}/L_{FIR}$ ratio and the star formation rate surface density, we find trends that agree with both the relation derived by Muñoz & Oh (2016), based on a thermal saturation of the [C II] emission, and that of Díaz-Santos et al. (2017), based on high radiation field strength to gas density ratios. It is therefore not possible at this stage to determine which of these models best explains the [C II] deficit.

Deeper [C II] observations with uv-coverage at long, medium, and short baselines are necessary to test the hypothesis that SMGs have smooth or clumpy structures, as well as to establish what physical processes drive the [C II] deficit.

ORCID iDs

A. M. Swinbank https://orcid.org/0000-0003-1192-5837
I. Smail https://orcid.org/0000-0003-3037-257X
F. Bertoldi https://orcid.org/0000-0002-1707-1775
C.-C. Chen https://orcid.org/0000-0002-3805-0789
E. A. Cooke https://orcid.org/0000-0003-3843-8393
K. E. K. Coppin https://orcid.org/0000-0002-0729-2988
H. Dannerbauer https://orcid.org/0000-0001-7147-3575
A. C. Edge https://orcid.org/0000-0002-3398-6916
D. Farrah https://orcid.org/0000-0003-1748-2010
T. R. Greve https://orcid.org/0000-0002-2554-1837
J. Hodge https://orcid.org/0000-0001-6586-8845
R. J. Ivison https://orcid.org/0000-0001-5118-1313
A. Karim https://orcid.org/0000-0002-8414-9579
E. Schinnerer https://orcid.org/0000-0002-3933-7677
D. Scott https://orcid.org/0000-0002-6878-9840
J. M. Simpson https://orcid.org/0000-0002-8521-1995
S. M. Stach https://orcid.org/0000-0003-1122-6948
F. Walter https://orcid.org/0000-0003-4793-7880
J. L. Wardlow https://orcid.org/0000-0003-2376-8971

References

ALMA Partnership, Vlahakis, C., Hunter, T. R., et al. 2015, ApJL, 808, L4
Armus, L., Mazzarella, J. M., Evans, A. S., et al. 2009, PASP, 121, 559
Bothwell, M. S., Smail, I., Chapman, S. C., et al. 2013, MNRAS, 429, 3047
Bournaud, F., Perret, V., Renaud, F., et al. 2014, ApJ, 780, 57
Brauher, J. R., Dale, D. A., & Helou, G. 2008, ApJS, 178, 280
Capak, P. L., Carilli, C., Jones, G., et al. 2015, Natur, 522, 455
Carniani, S., Marconi, A., Biggs, A., et al. 2013, A&A, 559, A29
Casey, C. M., Narayanan, D., & Cooray, A. 2014, PhR, 541, 45
Chapman, S. C., Blain, A. W., Smail, I., & Ivison, R. J. 2005, ApJ, 622, 772
Chapman, S. C., Smail, I., Blain, A. W., & Ivison, R. J. 2004, ApJ, 614, 671
Chen, C.-C., Smail, I., Swinbank, A. M., et al. 2015, ApJ, 799, 194
Clements, D. L., & Baker, A. C. 1996, A&A, 314, L5
Coppin, K. E. K., Smail, I., Alexander, D. M., et al. 2009, MNRAS, 395, 1905
Cowley, W. I., Béthermin, M., Lagos, C. d. P., et al. 2017, MNRAS, 467, 1231
Croxall, K. V., Smith, J. D., Pellegrini, E., et al. 2017, ApJ, 845, 96
Croxall, K. V., Smith, J. D., Wolfire, M. G., et al. 2012, ApJ, 747, 81
da Cunha, E., Groves, B., Walter, F., et al. 2013, ApJ, 766, 13
Dale, D. A., Beltz-Mohrmann, G. D., Egan, A. A., et al. 2016, AJ, 151, 4
De Breuck, C., Williams, R. J., Swinbank, M., et al. 2014, Msngr, 156, 38
Dekel, A., Sari, R., & Ceverino, D. 2009, ApJ, 703, 785
Díaz-Santos, T., Armus, L., Charmandaris, V., et al. 2013, ApJ, 774, 68
Díaz-Santos, T., Armus, L., Charmandaris, V., et al. 2017, ApJ, 846, 32
Díaz-Santos, T., Assef, R. J., Blain, A. W., et al. 2016, ApJL, 816, L6
Elmegreen, D. M., Elmegreen, B. G., Marcus, M. T., et al. 2009, ApJ, 701, 306
Engel, H., Tacconi, L. J., Davies, R. I., et al. 2010, ApJ, 724, 233
Faisst, A. L., Capak, P. L., Yan, L., et al. 2017, ApJ, 847, 21
Farrah, D., Lebouteiller, V., Spoon, H. W. W., et al. 2013, ApJ, 776, 38
Farrah, D., Rowan-Robinson, M., Oliver, S., et al. 2001, MNRAS, 326, 1333
Förster Schreiber, N. M., Shapley, A. E., Genzel, R., et al. 2011, ApJ, 739, 45
Geach, J. E., Dunlop, J. S., Halpern, M., et al. 2017, MNRAS, 465, 1789
Genzel, R., Tacconi, L. J., Combes, F., et al. 2012, ApJ, 746, 69
Graciá-Carpio, J., Sturm, E., Hailey-Dunsheath, S., et al. 2011, ApJL, 728, L7
Gullberg, B., De Breuck, C., Vieira, J. D., et al. 2015, MNRAS, 449, 2883
Hailey-Dunsheath, S., Nikola, T., Stacey, G. J., et al. 2010, ApJL, 714, L162
Hatsukade, B., Tamura, Y., Iono, D., et al. 2015, PASJ, 67, 93
Hayward, C. C., Kereš, D., Jonsson, P., et al. 2011, ApJ, 743, 159
Hill, T., Burton, M. G., Minier, V., et al. 2005, MNRAS, 363, 405
Hodge, J. A., Karim, A., Smail, I., et al. 2013, ApJ, 768, 91
Hodge, J. A., Swinbank, A. M., Simpson, J. M., et al. 2016, ApJ, 833, 103
Ikarashi, S., Ivison, R. J., Caputi, K. I., et al. 2015, ApJ, 810, 133
Iono, D., Yun, M. S., Aretxaga, I., et al. 2016, ApJL, 829, L10
Ivison, R. J., Smail, I., Amblard, A., et al. 2012, MNRAS, 425, 1320
Ivison, R. J., Swinbank, A. M., Swinyard, B., et al. 2010, A&A, 518, L35
James, A., Dunne, L., Eales, S., & Edmunds, M. G. 2002, MNRAS, 335, 753
Jones, G. C., Willott, C. J., Carilli, C. L., et al. 2017, ApJ, 845, 175
Kennicutt, R. C., Calzetti, D., Aniano, G., et al. 2011, PASP, 123, 1347
Kennicutt, R. C., Jr. 1998, ARA&A, 36, 189
Kennicutt, R. C., Jr., & Chu, Y.-H. 1988, AJ, 95, 720
Kimball, A. E., Lacy, M., Lonsdale, C. J., & Macquart, J.-P. 2015, MNRAS, 452, 88
Lagache, G., Cousin, M., & Chatzikos, M. 2018, A&A, 609, 130
Law, D. R., Steidel, C. C., Erb, D. K., et al. 2009, ApJ, 697, 2057
Livermore, R. C., Jones, T., Richard, J., et al. 2012, MNRAS, 427, 688
Lord, S., Malhotra, S., Helou, G., et al. 1996, BAAS, 28, 929
Luhman, M. L., Satyapal, S., Fischer, J., et al. 1998, ApJL, 504, L11
Luhman, M. L., Satyapal, S., Fischer, J., et al. 2003, ApJ, 594, 758
Lutz, D., Berta, S., Contursi, A., et al. 2016, A&A, 591, A136
Madden, S. C., Geis, N., Genzel, R., et al. 1993, ApJ, 407, 579
Magdis, G. E., Rigopoulou, D., Hopwood, R., et al. 2014, ApJ, 796, 63
Malhotra, S. 2001, in ESA Special Publication 460, The Promise of the Herschel Space Observatory, ed. G. L. Pilbratt et al. (Paris: ESA), 155
Malhotra, S., Helou, G., Stacey, G., et al. 1997, ApJL, 491, L27
McMullin, J. P., Waters, B., Schiebel, D., Young, W., & Golap, K. 2007, in ASP Conf. Ser. 376, Astronomical Data Analysis Software and Systems XVI, ed. R. A. Shaw, F. Hill, & D. J. Bell (San Francisco, CA: ASP), 127
Muñoz, J. A., & Oh, S. P. 2016, MNRAS, 463, 2085
Nesvadba, N., Kneissl, R., Cañameras, R., et al. 2016, A&A, 593, L2
Oteo, I., Zwaan, M. A., Ivison, R. J., Smail, I., & Biggs, A. D. 2017, ApJ, 837, 182
Riechers, D. A., Cooray, A., Omont, A., et al. 2011, ApJL, 733, L12
Sakamoto, K., Wang, J., Wiedner, M. C., et al. 2008, ApJ, 684, 957
Sanders, D. B., & Mirabel, I. F. 1996, ARA&A, 34, 749
Shibuya, T., Ouchi, M., & Harikane, Y. 2015, ApJS, 219, 15
Simpson, J. M., Smail, I., Swinbank, A. M., et al. 2015a, ApJ, 807, 128
Simpson, J. M., Smail, I., Swinbank, A. M., et al. 2015b, ApJ, 799, 81
Simpson, J. M., Smail, I., Swinbank, A. M., et al. 2017, ApJ, 839, 58
Smith, J. D. T., Croxall, K., Draine, B., et al. 2017, ApJ, 834, 5
Stacey, G. J., Geis, N., Genzel, R., et al. 1991, ApJ, 373, 423
Stacey, G. J., Hailey-Dunsheath, S., Ferkinhoff, C., et al. 2010, ApJ, 724, 957
Surace, J. A., Sanders, D. B., & Evans, A. S. 2001, AJ, 122, 2791
Swinbank, A. M., Dye, S., Nightingale, J. W., et al. 2015, ApJL, 806, L17
Swinbank, A. M., Karim, A., Smail, I., et al. 2012, MNRAS, 427, 1066
Swinbank, A. M., Simpson, J. M., Smail, I., et al. 2014, MNRAS, 438, 1267
Swinbank, A. M., Smail, I., Longmore, S., et al. 2010, Natur, 464, 733
Tacconi, L. J., Genzel, R., Saintonge, A., et al. 2018, ApJ, 853, 179
Tacconi, L. J., Genzel, R., Smail, I., et al. 2008, ApJ, 680, 246
Toomre, A. 1964, ApJ, 139, 1217
Umehata, H., Matsuda, Y., Tamura, Y., et al. 2017, ApJL, 834, L16
Valtchanov, I., Virdee, J., Ivison, R. J., et al. 2011, MNRAS, 415, 3473
Veilleux, S. 2002, in ASP Conf. Ser. 254, Extragalactic Gas at Low Redshift, ed. J. S. Mulchaey & J. T. Stocke (San Francisco, CA: ASP), 313
Venemans, B. P., Walter, F., Decarli, R., et al. 2017, ApJ, 837, 146
Wang, R., Wagg, J., Carilli, C. L., et al. 2013, ApJ, 773, 44
Weiß, A., De Breuck, C., Marrone, D. P., et al. 2013, ApJ, 767, 88
Weiß, A., Kovács, A., Coppin, K., et al. 2009, ApJ, 707, 1201
Younger, J. D., Fazio, G. G., Wilner, D. J., et al. 2008, ApJ, 688, 59
Zhang, Z.-Y., Papadopoulos, P. P., Ivison, R. J., et al. 2016, RSOS, 3, 160025